Hopkins-Skellam index and origin of spatial regularity in InAs quantum dot formation on GaAs(001)

Tomoya Konishi,[1,a)] Gavin R. Bell,[2] and Shiro Tsukamoto[1]
[1]*Centre for Collaborative Research, National Institute of Technology, Anan College, Anan, Tokushima 774-0017, Japan*
[2]*Department of Physics, University of Warwick, Coventry CV47AL, United Kingdom*

(Received 24 December 2014; accepted 29 March 2015; published online 13 April 2015)

We investigate the origin of the spatial regularity of arrays of InAs quantum dots (QDs) grown on GaAs(001). The Hopkins-Skellam index (HSI) is used with a newly developed calculation algorithm to quantify the spatial regularity both of QDs and of nm-sized surface reconstruction territories (SRTs) present in the $In_xGa_{1-x}As$ wetting layer prior to QD nucleation. The SRT is the minimum extent of a surface reconstruction region needed for one QD to nucleate. By computing the evolving HSI of SRTs from sequences of *in situ* scanning tunnelling microscopy images during growth, we find that the spatial regularity of QDs is traced back to that of the $(n \times 3)$ SRTs as early as 0.6 monolayers of InAs coverage. This regularity is disturbed by the $(n \times 4)$ SRTs which appear at higher coverage. The SRT approach is discussed in comparison to conventional capture zone theories of surface growth. © *2015 AIP Publishing LLC*. [http://dx.doi.org/10.1063/1.4917213]

I. INTRODUCTION

Spatial regularity is a fundamental statistical property of arrays of objects. Spatial distributions in two dimensions may be highly regular or completely random or have some quasi-regular or clustered character. Various measures can be used to characterise spatial regularity: in the life sciences, the Hopkins-Skellam index (HSI) has been widely applied to analyse distribution of individuals in a plant population,[1] nesting pattern of grey gulls on a beach,[2] distribution of epidermal Langerhans cells in human skin,[3] and distribution of forest stands.[4] In the physical sciences, the HSI appears not to be widely known. Nucleation and growth at surfaces is a long-studied field with strong current importance in nanomaterials development[5,6] and two-dimensional materials production. For example, in the scalable growth of graphene on spatially non-uniform metal surfaces,[7] the spatial distribution of graphene grains must influence the nature of grain boundaries, which in turn limit the electrical conductivity of the graphene sheet.[8] In the present work, we apply the HSI to analyse the spatial regularity of self-assembled semiconductor nanostructures.

Semiconductor quantum dots (QDs) attract enormous attention as the nano-materials basis for lasers[9] and next-generation solar cells.[10,11] These QDs are nano-scale particles of conventional semiconductor materials (commonly InAs) which can be formed by self-assembly of 3D islands on a 2D semiconductor substrate (commonly GaAs). This allows formation of QD arrays with extremely high quality and in one continuous epitaxial growth run. The 3D islands form on a 2D wetting layer (WL) of the semiconductor surface at high temperatures. While this method is simple and popular, it remains difficult to arrange QDs in a dense and uniform array for optimal use in devices.[12] The low density limit of QD self-assembly may be valuable in developing quantum information processing: control of spatial regularity is important to allow pairs of interacting QDs to act as a qubit.[13] In order to overcome these drawbacks, it is necessary to understand in detail the mechanism of QD nucleation. In particular, it is important to elucidate the nature of the WL as a scaffold of QD nucleation.[14]

Instead of interrupting growth to image sample surfaces outside the growth chamber at room temperature,[14] our custom-built system allows a scanning tunnelling microscope (STM) instrument to enter an ultra-high vacuum molecular beam epitaxy (MBE) chamber, giving genuinely integrated STMBE capability.[15] In the InAs-GaAs system, the WL is an $In_xGa_{1-x}As$ alloy with complex surface reconstructions which evolve during its growth.[16] The structure is a directly visible aspect of the alloy fluctuations.

In our previous study,[17] in order to understand how QD nucleation is triggered by the surface alloy fluctuations, we compared the spatial distributions of the surface reconstructions and that of QD nucleation sites. The spatial distribution was characterised by calculating the cumulative probability function, $F(d)$, of the distance to the nearest neighbouring individual from a randomly selected location, and is significantly more regular than a random (Poisson) distribution. From the similarity of $F(d)$ traces and densities, we concluded that QD nucleation pattern is more reflected by the distribution of $(n \times 3)$ than that of $(n \times 4)$. This implied that QD nucleation was induced on $(n \times 3)$ rather than $(n \times 4)$ regions, i.e., the QD nucleation pattern was determined by the distribution of $(n \times 3)$ surface reconstruction. This provided an important clue to the control of the spatial pattern of QD nucleation by surface engineering the WL. However, for this purpose, it is necessary to understand how the distribution of $(n \times 3)$ surface reconstruction *evolves* in the course of WL growth. Our previous results could not address this point because we analysed only one STM image of the WL

a)Electronic mail: konishi@anan-nct.ac.jp. Telephone/FAX: (+81) 884 23 7254.

which was acquired after interrupting the MBE growth at 430 °C and cooling down to 300 °C.[17]

In the present study, we go far beyond this previous work and directly attack the problem of WL evolution. By carefully analysing image sequences of particular areas of the sample surface during MBE growth, at 430 °C acquired by using STMBE,[16] we are able to extract the time evolution of the surface area of $(n \times 3)$ reconstruction. For each frame of the image sequence, we located the regions of $(n \times 3)$ surface reconstruction by measuring As dimer row pitches, and characterised the spatial distribution of patches of $(n \times 3)$ reconstructed surface by using nearest-neighbour analysis. Here, we firstly introduce the HSI to characterise the spatial distribution of $(n \times 3)$ reconstruction more precisely than our previous study. We discuss the implications for WL engineering to enhance the regularity and density of self-assembled InAs-GaAs QDs.

II. THEORETICAL BACKGROUND

A. Hopkins-Skellam index

In this study, we introduce the HSI[1] to describe the type of spatial distribution of points, for example, regular, random, and aggregated. The type of spatial distribution can be discussed by computing the $F(d)$ functions of point patterns and comparing their traces.[17] However, HSI gives more concrete information of spatial ordering and enables precise comparison. Despite its broad application in life sciences, we are not aware of HSI being widely used in surface growth. HSI is calculated by nearest-neighbour analysis of points as follows:

$$\mathrm{HSI} = \sum_{i=1}^{N} {r_{1i}}^2 \Big/ \sum_{i=1}^{N} {r_{2i}}^2. \tag{1}$$

Here, r_{1i} denotes the distance to the nearest point from a randomly selected location in the study region R of area A. Similarly, r_{2i} denotes the distance to the nearest point from the i-th point, and N is the total number of points. The HSI equals 1 when a set of points is perfectly random (ideal Poisson pattern) because selecting a random location is equivalent to selecting a member of a set of randomly located points. On the other hand, when points are strongly aggregated, the distance r_1 from a randomly selected location to the closest point tends to be larger than the separation between points, hence the HSI is greater than 1. The minimum value of HSI occurs for perfectly ordered point patterns such as a hexagonal lattice. The HSI of a hexagonal lattice was calculated to be 0.14, which was consistent with the theoretical minimum of 5/36. For point patterns of intermediate regularity, the HSI increases from 0.14 towards 1 as the randomness increases, and allows such arrays to be distinguished even when inspection by eye reveals no obvious difference. Example arrays are shown in Fig. 1.

Since the computation of HSI is usually based on a simulation selecting random locations to compute r_{1i}, its accuracy is dependent on the number of trials. The definition of HSI requires the number of randomly selected locations in each trial to equal the number of points in the pattern, hence each trial will probably not "see" every point and slightly different values of HSI will be produced. The number of trials required to converge the HSI to a given significant digit increases rapidly. For example, the arrays in Fig. 1 have around 80 points and to calculate the HSI to 2 significant figures takes around 10^5 trials and 2 hours on a standard desktop machine. This can be made more efficient by adopting the following algorithm, where random plotting simulation is not used.

When the trial number is sufficient, the numerator of Eq. (1) converges to the expected value of ${r_1}^2$ multiplied by N. The expected value, $\langle {r_1}^2 \rangle$, is easily computed by the derivative of $F(d)$ function, that is, the probability function of normalised r_1. The $F(d)$ function itself can be calculated straightforwardly using the method outlined in Ref. 17.

Now the HSI is given by

$$\mathrm{HSI} = N\langle {r_1}^2 \rangle \Big/ \sum_{i=1}^{N} {r_{2i}}^2, \tag{2}$$

$$= N \int_0^\infty (fd)^2 F'(d)\, \mathrm{d}d \Big/ \sum_{i=1}^{N} {r_{2i}}^2, \tag{3}$$

$$= A \int_0^\infty d^2 F'(d)\, \mathrm{d}d \Big/ \sum_{i=1}^{N} {r_{2i}}^2, \tag{4}$$

where f is the factor to calculate the normalised distance d as given by

$$f = \sqrt{A/N}. \tag{5}$$

In this case, the accuracy depends on the resolution of d to calculate $F(d)$ function[17] but requires much less computational cost than the simulation method. For example, the HSI for the arrays in Fig. 1 could be calculated to 3 significant digits in around 2 min.

Figure 1 shows examples of point patterns, starting from a hexagonal lattice, which is most regular in the 2D space, to more random patterns by adding some noise, and the computed HSI values.

B. Surface reconstruction territory (SRT)

The local surface reconstruction types on InAs-GaAs(001) form a patch-like island structure. Since it was suggested that QD nucleation occurs in $(n \times 3)$ surface reconstruction region,[16,17] we assume a minimum extent of $(n \times 3)$ surface reconstructed region which is needed to support one QD nucleation. In our previous study,[17] the size and shape of the region were determined a priori, for example, an oval including four neighbouring unit cells of a surface reconstruction. Here, the size and the shape are determined using a rational procedure based on the statistics of QDs. The density and the spatial distribution of these regions reflect those of QD nucleation sites. We call the optimally determined region a "SRT." Since the concept of the SRT is based on QD nucleation, the shape and size of SRT depend on the growth conditions. The shape of an SRT is not well

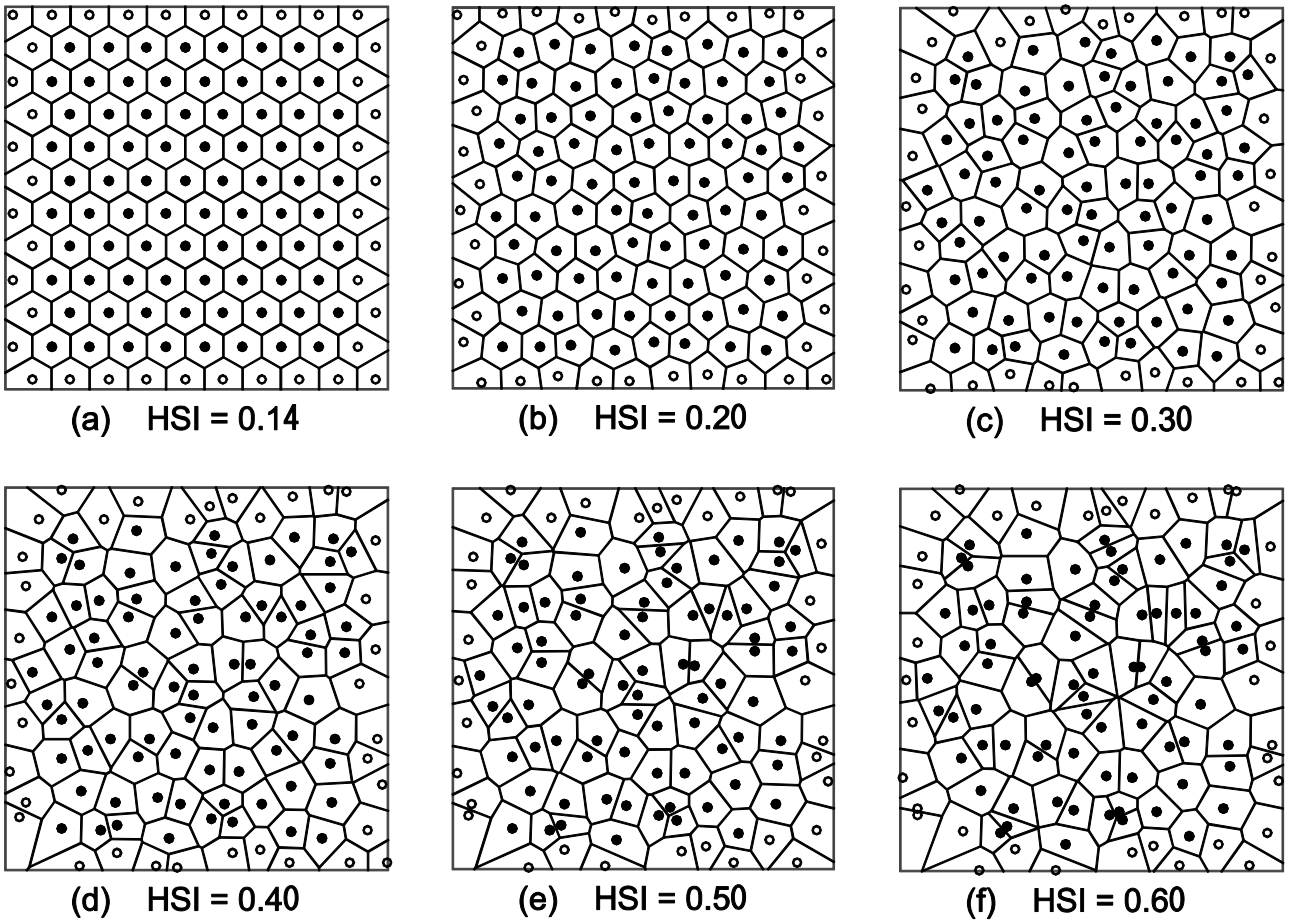

FIG. 1. Perturbation of a hexagonal lattice and the computed HSI. Points denoted by open markers are not used to compute HSI since belonging Voronoi cells touch study regions sides.

defined, and different shapes could co-exist while supporting one QD nucleation event per SRT, but we assumed a single shape in our calculation for simplicity. We used rectangular SRTs, with a length L and a width W, to account for the anisotropic diffusion of In on the $(n \times 3)$- and $(n \times 4)$-reconstructed As dimer row structures.[18–22] Multiple SRTs can lie adjacent on the surface as part of a larger contiguous reconstruction domain but the SRTs may not overlap each other. However, because a rigid rectangular SRT does not reflect the possible diversity of SRT shapes, we allow overlaps to absorb the difference between a realistic undefined shape and the assumed rectangular shape. Here, we introduce the overlap parameter, P_{OL}, to restrict the overlapped fraction of SRT to $1 - P_{OL}$. The SRTs for different reconstruction pitches are assigned to each STMBE image by a simple Monte Carlo (MC) method. This positions each new SRT randomly and accepts it if the SRT covers a minimum fractional area (P_{OL}) of the desired pitch range, counting existing SRT areas as unavailable. The SRT size (L and W) and P_{OL} are the only free parameters of the assignment process. They are optimised by repeating the assignment process until the spatial density and distribution of SRTs resemble those of QDs. Hence the minimal surface area to allow nucleation of one QD is P_{OL} times the rectangle area, and the procedure allows some flexibility in the shape of the resulting SRTs without introducing many arbitrary parameters.

III. METHODOLOGY

A. Pre-processing of STMBE images

The surface images of InAs-GaAs(001) WL were reported using STMBE scanning during the growth where InAs was deposited at a rate of 2.5×10^{-4} ML s^{-1} with a substrate temperature of 430 °C and an As_4 flux of $(1.5 \pm 0.5) \times 10^{14}$ molecules $cm^{-2}\,s^{-1}$ as described in the literature.[16] In this study, we newly processed and analysed all of the STMBE images including those unreported. Image processing of the STMBE data was performed using a home-made programme. Each frame of the STMBE sequence is (1) translated relative to its predecessor and (2) shear-distorted, because of inevitable thermal drift during 200 s image acquisition time. All of the images were mutually registered after the STMBE runs, and also shear-transformed so that dimer rows were oriented vertically on the images. This was done using an affine transform with control points selected on static pit defects. The registered images were cropped to a $42 \times 42\,nm^2$ (420×420 pixels) study region common to all the images (Fig. 2(a)). STMBE images acquired at high temperatures always appear "scratched" (with scan-line noise) because of rapidly migrating In adatoms on the surface, but images clearly show the stripes. This scan-line noise is one of the most serious factors to affect measurement accuracy. Since the frequency of the noise is higher than that of dimer

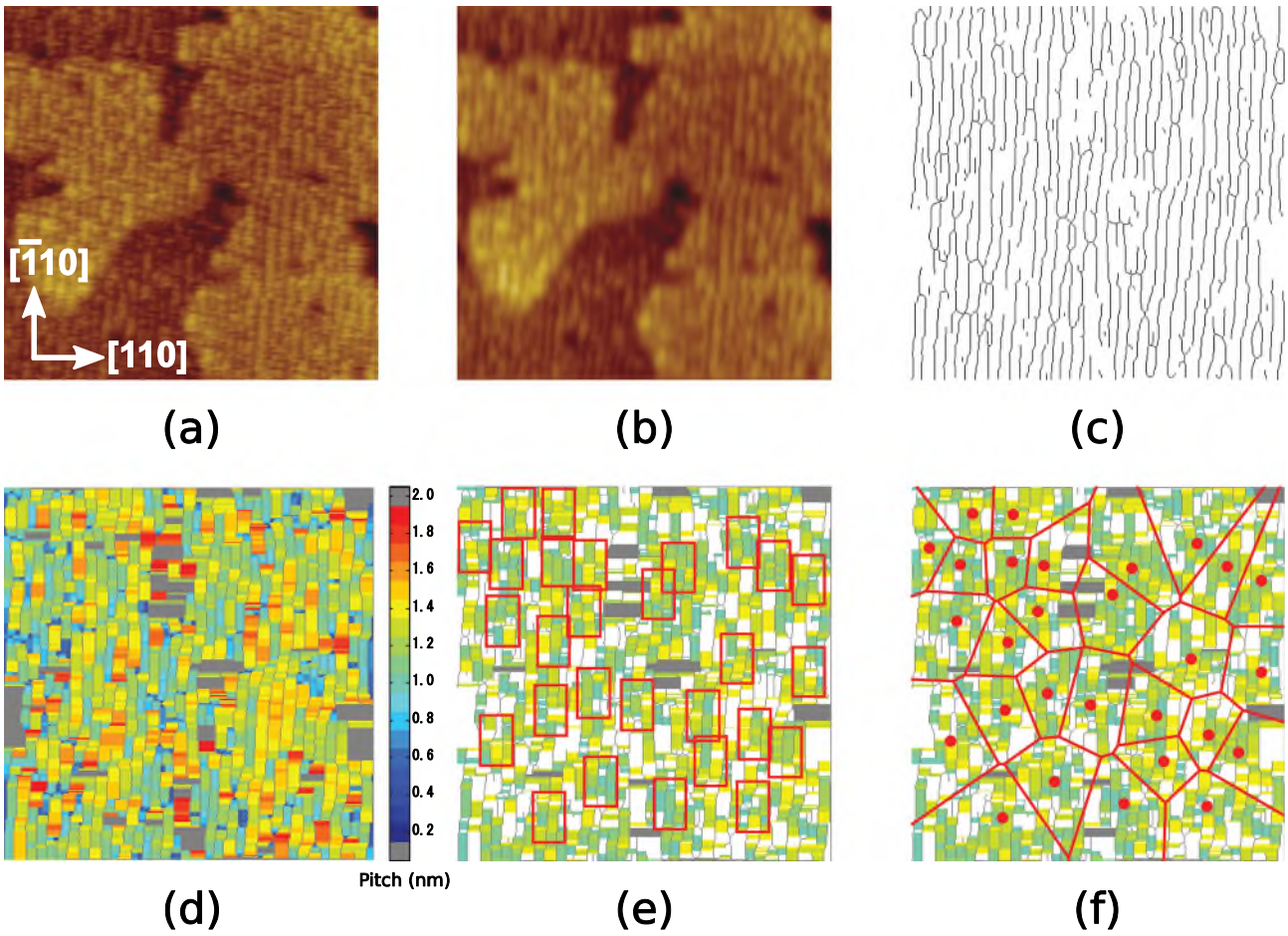

FIG. 2. Steps in image processing of STMBE data. A typical 42 nm STMBE image is shown in (a) and subsequent steps are described in the text.

row periodicity, the noise was effectively removed but the [110] pitch was faithfully preserved using low-pass filtering by moving average and fast Fourier transform (FFT) convolution (Fig. 2(b)). For each image, the background slope was carefully subtracted. A horizontal raster profile across the stripes was then scanned to find local maximal points and to plot them on a corresponding black and white image. Repeating the procedure for all the scan lines of the STMBE image, we thus obtained a map of ridgelines in Fig. 2(c). The ridgelines represent the topographical maxima associated with the local surface reconstruction, most likely to be the As dimer rows.[16,17,21,23] Dynamic imaging *in situ* does not allow resolution of individual As dimers, but the distance between ridgelines ("pitch") lets us infer the local reconstruction periodicity, as described below. The map contained some isolated dots and "wire-cutting" noise, which were cleaned by dilation and erosion image processing.

B. Surface reconstruction analysis of STMBE images

A map of ridgeline pitch (Fig. 2(d)) was obtained by counting pixels between the ridgelines using a homemade programme. The pitch, as the extent of the unit mesh along [110] direction, allows us to distinguish between locally reconstructed $(n \times 2)$, $(n \times 3)$ and $(n \times 4)$ regions of the WL surface.[16,17,21,23] Here, only pixels belonging to a certain range of pitch, for example, 1.0–1.4 nm for an $(n \times 3)$ surface reconstruction allowing for dynamic imaging effects, were highlighted in the pitch map.

We then assigned SRTs on the last frame of STMBE sequence by a simple MC method, as follows. First a rectangle of L and W was randomly placed on the map. If the rectangle covered a minimum fraction (P_{OL}) of the highlighted pixels, the rectangle was accepted as SRT and the covered pixels were un-highlighted as unavailable area in the map. This operation was repeated until no new SRT was located on the map any more (Fig. 2(e)).

We repeated the assignment of SRTs using rough grid sets of free parameters with spacing of 0.05 for P_{OL}, and 0.5 nm for L and W. Then the grid sets were filtered to give the density of SRTs approaching that of QDs, $(0.96–1.7) \times 10^{12}\,\mathrm{cm}^{-2}$.[17] The error was comparable to typical variation of SRTs density within 10 runs of SRTs assignment simulations. The density of QDs were precisely measured by processing the STMBE image of QDs in Ref. 16. It is well known that the areal density of QDs is at most $\sim 10^{10}\,\mathrm{cm}^{-2}$ with the lateral size of ~ 30 nm under the typical growth temperature of 500 °C.[24] However, we used the STMBE images of InAs surface growing at the low growth rate and 430 °C for high-resolution scanning.[16] Consequently, the mean width of QDs was 7.5 nm and the areal density of QDs reached $\sim 10^{12}\,\mathrm{cm}^{-2}$ which was unusually high for the MBE growth of InAs on GaAs.

Next the filtered free parameters, P_{OL}, L, and W, were tuned by comparing the spatial distribution of SRTs with

those of QDs under the ansatz that SRTs of a certain pitch seed QD nucleation. For the comparison, we used the correlation of $F(d)$ function, which is the cumulative probability function of point-random point nearest neighbour distance. First the study region was subjected to Voronoi tessellation using the coordinates of SRTs as shown in Fig. 2(f). The profile of $F(d)$ was calculated by summing up each common area of a circle, of radius d and centred at SRT, and the belonging Voronoi cell.[17] The $F(d)$ function of QDs was calculated as well using the Voronoi tessellation of the STMBE image of QDs. A run of the MC simulation using a certain set of free parameters gave a different pattern of SRTs and hence a different form of $F(d)$ function. We again repeated the SRT assignment process, tuning the parameter set to minimise the residual sum of squares (RSS) in correlating $F(d)$ function of SRTs and that of QD nucleation sites and the error of spatial densities. Using the optimised parameter set, assignments of SRTs were performed throughout all the images to visualise the dynamic change of surface reconstruction during $In_xGa_{1-x}As$ 2D growth.

IV. RESULTS AND DISCUSSION

A. Assignment and optimisation of SRTs

The continuous STMBE observation was performed in a single region of the substrate throughout the growth, but inevitable thermal drift in the STMBE shifts the image from frame to frame and induces slight image distortion. Therefore, the images were registered and cropped to focus on smaller regions common to all the STMBE images in a single run. The analysis shown here focuses on a previously published STMBE sequence[16] where remarkably slow drift enabled a long sequence of registered $42 \times 42\,nm^2$ STMBE images to be obtained with low distortion. Example STMBE images of typical growth stages A–D, described in Sec. IV C, are shown in Fig. 3(left side column).

All of the images showed clear stripes of surface reconstruction. For each *in situ* STM image of Fig. 3, regions of $(n \times 3)$ reconstruction pitch $(1.2 \pm 0.2\,nm)$ were located and results are shown in Fig. 3(right side column) as colour-coded maps. From frame to frame, different patterns of $(n \times 3)$ pitch appeared. In terms of total coverage of the different pitches, the overall evolution is from $(n \times 2)$ to $(n \times 3)$ to $(n \times 4)$, in agreement with the average pitch measured by both Fourier transforms along [110] of the STMBE images[16] and the measured position of the fractional order streak in RHEED.[16,25] This confirms the reliability of the pitch extraction. When successive frames are examined, there is no correlation between domain positions, as shown in the right side column of Fig. 3. This strikingly evidents in an STMBE movie of Fig. 4. Domains $<10\,nm$ in size appear and disappear from frame to frame, indicating a facile transition between locally $(n \times 3)$ and $(n \times 4)$ reconstructions. These two reconstructions share an As dimer row structure (the stripes seen in STMBE images) and readily co-exist[19,25,26] with kink structures in the dimer rows.[27] Importantly, steady growth of new domains does not occur and the local structure of the 2D alloy layer is highly dynamic.

Next, we repeated the MC assignment of SRTs on the $(n \times 3)$ pitch map of the last STMBE images using rough grid sets of free parameters, P_{OL}, L and W. The overlap parameter, P_{OL}, was then determined to be 0.7 since it allowed more combinations of filtered L and W where the density of the SRTs targets that of QDs. The size of SRTs was optimised to $L = 5.5\,nm$ and $W = 3.5\,nm$ (corresponding to 13.75×8.75 GaAs mesh along $[\bar{1}10]$ and [110] directions, respectively), which yielded the most similar $F(d)$ trace to that of QDs. The variations of L and W within the range of $\pm 0.5\,nm$ gave the same order of RSS in the correlation of $F(d)$ functions. Typical SRT assignments for the $(n \times 3)$ reconstruction using the optimised parameter set are shown in Fig. 3 (right column). In contrast, no $(n \times 4)$ SRTs could be assigned to give similar results to the QDs. In order to investigate how $(n \times 3)$ SRTs, which seed QD nucleations, are developed throughout the WL growth, we assigned $(n \times 3)$ SRTs, using the optimised parameter set, in each frame of STMBE sequence.

B. Statistical correlation between SRTs and QD nucleation sites

Once a $(n \times 3)$ SRT map is obtained, the $F(d)$ function, which characterise the distribution of the SRTs, is readily calculated via Voronoi tessellation of the SRT map. For each frame of STMBE images, assignment of $(n \times 3)$ SRTs was tried for 10 times. Each run of the MC assignment produces a different array of SRTs on a given reconstruction domain pattern and a statistical envelope of $F(d)$ curves can be built to give reliable error bars. In Fig. 5 we show $F(d)$ traces of the $(n \times 3)$ SRTs calculated for each stage of WL growth (these stages are discussed later) along with those of QDs. The trace of the $(n \times 3)$ SRTs was plotted with error bars based on 10 trials of the MC SRT assignments. The trace of QDs was plotted as an envelope comprising the results from 9 different regions of $333 \times 333\,nm^2$ of this sample, imaged at InAs coverage beyond the critical thickness. For reference, we also show the $F(d)$ traces for a regular grid of points (blue line) and random scatters of points with Poisson distribution (yellow envelope). The QD spatial pattern lies somewhere between ordered and random. In order to visualise the change of $(n \times 3)$ SRT traces, the envelope of QD traces is shown for each stages A–D as an guide to the eye. At very low InAs coverage (stage A), the trace of the $(n \times 3)$ SRTs is Poissonian. However, this quickly evolves to a trace which then lies within the envelope of the QD $F(d)$ traces. Furthermore, the areal densities of QDs and $(n \times 3)$ SRTs prior to the critical thickness match well (Fig. 6(b)). This suggests that QD nucleation is induced by $(n \times 3)$ SRTs where In adatoms accumulate to form an embryo 3D island. In other words, QDs originate in fleeting $(n \times 3)$ SRTs which randomly form and dissolve via the migration of adatoms in the highly dynamic WL.

Figure 6 shows the time evolution with InAs coverage of (a) "spatial occupancy," along with the frequency of surface reconstruction pitch by a contour plot. The spatial occupancy is defined as the ratio of $(n \times 3)$-reconstructed area to the total area. They show that rapid increase in the $(n \times 3)$

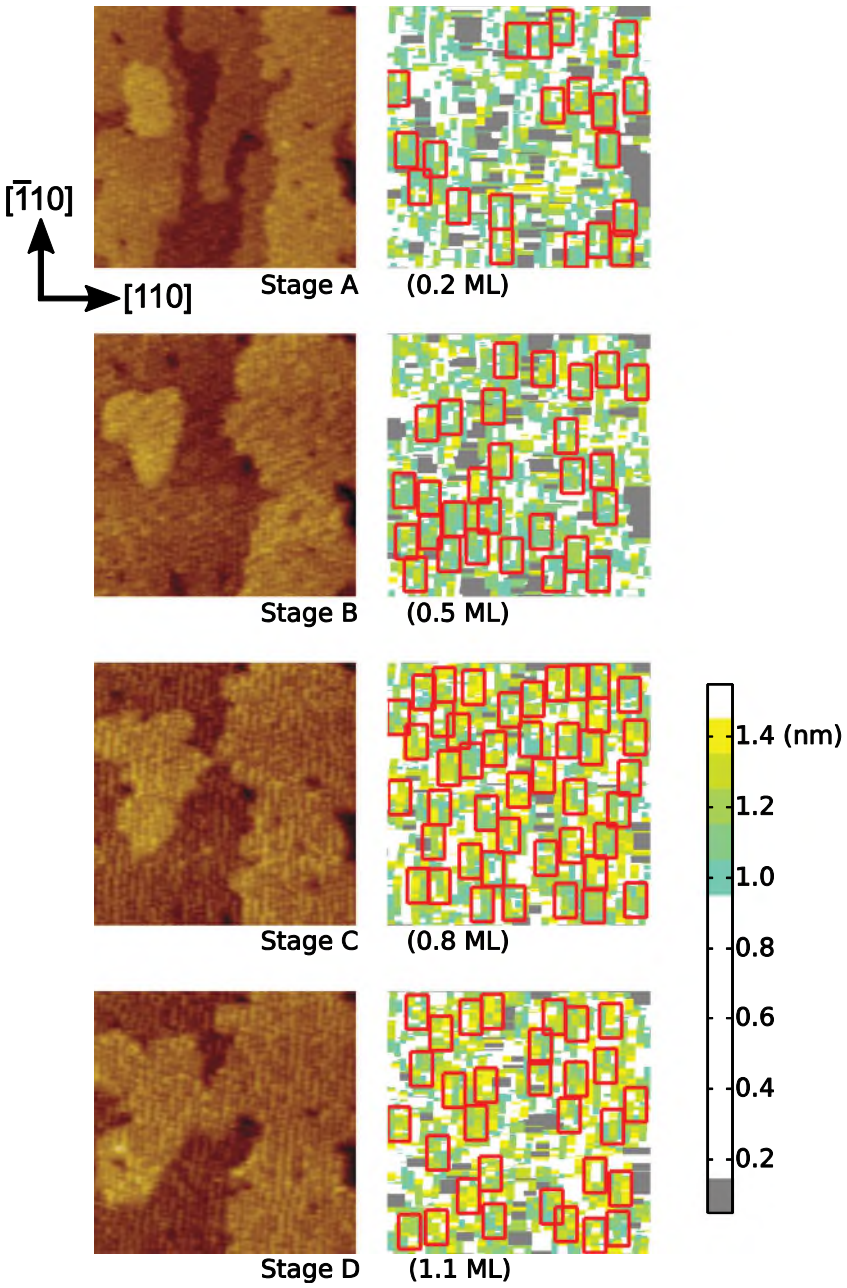

FIG. 3. Left side column shows $42 \times 42\,\text{nm}^2$ *in situ* STMBE images of InAs-GaAs(001) representing four typical growth stages A–D, respectively, as described in the text. The right side column shows $42 \times 42\,\text{nm}^2$ colour-coded maps of As-dimer row pitch of their respective STMBE images. Only regions where pitch is $1.2 \pm 0.2\,\text{nm}$, corresponding to $(n \times 3)$ surface reconstruction, are plotted. Regions where pitch is undetectable are plotted with grey. Typical assignment of SRTs on $1.2 \pm 0.2\,\text{nm}$ pitch is also indicated by red rectangular markers. The InAs coverage is printed below each pair.

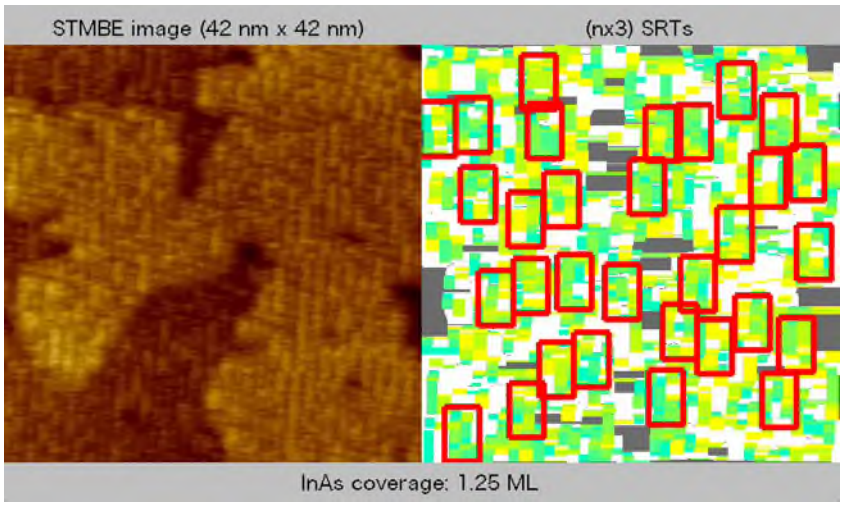

FIG. 4. $42 \times 42\,\text{nm}^2$ STMBE images of InAs-GaAs(001) during growth from 0.10 ML to 1.25 ML (left) and typical $(n \times 3)$ SRT allocation on the corresponding colour-coded maps of As-dimer pitch (right). Refer to Fig. 3 for the colour-scale bar. (Multimedia view) [URL: http://dx.doi.org/10.1063/1.4917213.1]

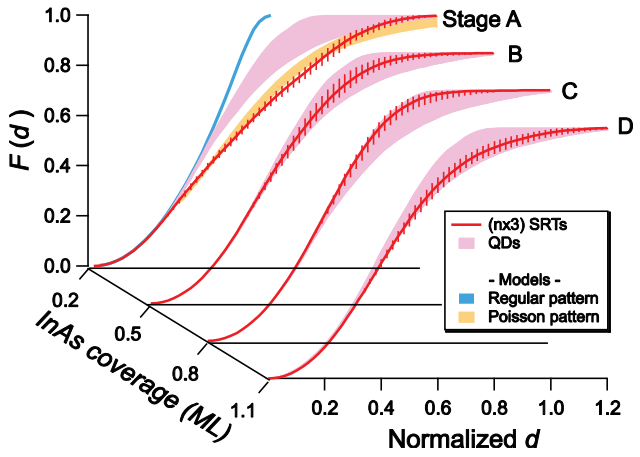

FIG. 5. Comparison of spatial distribution between $(n \times 3)$ SRTs and QDs. Traces of $F(d)$ functions of $(n \times 3)$ SRTs at four typical growth stages A–D are shown along with those of QDs for reference. $(n \times 3)$ SRTs were assigned by simple MC simulation with the best size and overlap parameter where the density becomes most similar to that of QDs. Error bars of $(n \times 3)$ SRTs indicate variation of 10 runs of simulation. $F(d)$ functions of QDs were measured in 9 different regions and their traces are plotted as an envelope. $F(d)$ trace of regular grid of points (blue) and envelope of random scatter points by 50 runs of MC simulations (yellow) are also plotted.

surface reconstruction occupancy at stage A and the gradual decrease after stage C. Figure 6 also shows (b) the SRT areal density of the $(n \times 3)$ surface reconstruction, and (c) HSI of the $(n \times 3)$ SRTs. They plot 10 markers at each step of InAs coverage corresponding to 10 results of SRTs assignment simulation.

In Fig. 6(b), the initial areal density of $(n \times 3)$ SRTs at ~0.2 ML is low. This is despite the substantial surface coverage of $(n \times 3)$ pitch even at 0.2 ML (indicated by the blue-green-yellow areas in Fig. 3). At low InAs coverage, the $(n \times 3)$ region was fragmented to small pieces and SRTs could not be assigned due to the overlap parameter threshold. The subsequent rapid rise in both spatial occupancy and SRT areal density (Figs. 6(a) and 6(b)) implies that small $(n \times 3)$ regions either grow or connect more effectively to form well-defined SRTs. It has been reported[28] that in the early stage of WL growth In atoms are immediately incorporated into the lattice of the WL, and the $(n \times 3)$ surface reconstruction forms quickly by intermixing of substrate Ga atoms into the WL. This concept is in agreement with the present results. We further find that the increase of $(n \times 3)$ areal density saturates at ~0.6 ML (Figs. 6(a) and 6(b)). This means that almost all of the surface supports $(n \times 3)$ reconstruction because the ideal $(n \times 3)$ surface reconstruction contains 66% of In.[21,25,26,29] After 0.9 ML of the InAs coverage, the $(n \times 3)$ SRT areal density begin to decrease. This indicates that $(n \times 3)$ surface reconstruction was replaced by $(n \times 4)$ surface reconstruction but with a slower rate than that of the initial increase. In the latter stage of WL growth, In atoms stick on $(n \times 3)$ As dimer row to form $(n \times 4)$ surface reconstruction. However, arriving In atoms do not always stick to the As dimer row but accumulate on the surface as rapidly migrating In adatoms.[16] Similar transitions at ~0.6 ML and ~0.9 ML were also reported for Fourier transforms along [110] of STMBE images[16] and in the streak patterns of reflection high-energy electron diffraction (RHEED).[16,25]

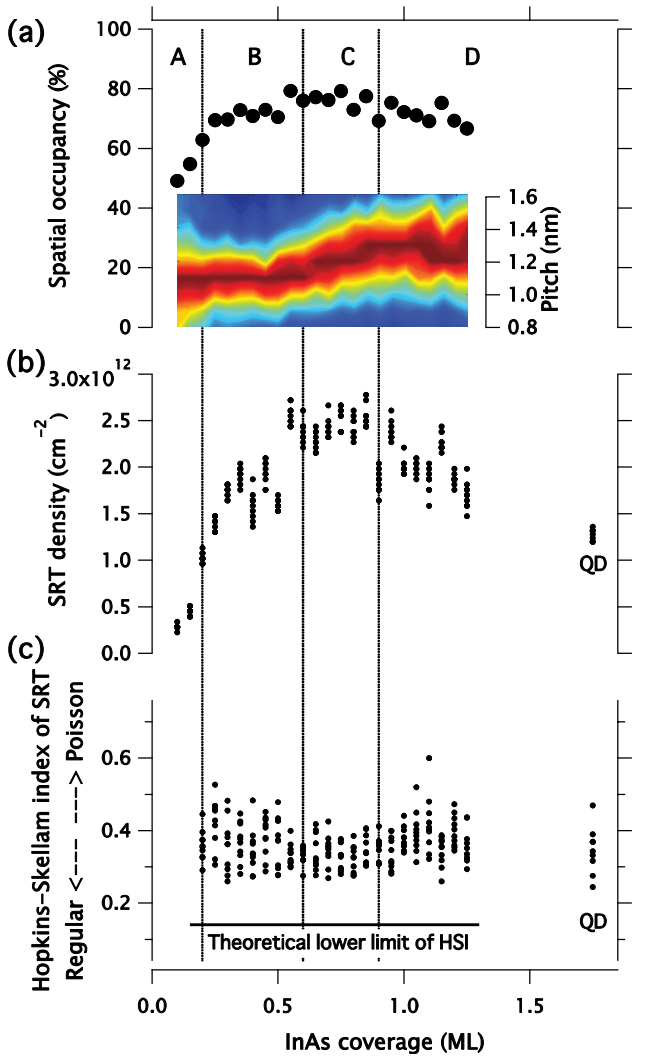

FIG. 6. Time evolution with InAs coverage of (a) the spatial occupancy of $(n \times 3)$-reconstructed surface and (b) the $(n \times 3)$ SRT areal density. (c) Hopkins-Skellam index (HSI) of $(n \times 3)$ SRTs as a function of InAs coverage. The density and HSI for a $T_{sub} = 430\,^{\circ}C$ QD array are also plotted at 1.75 ML. Background dotted lines divide typical growth stages (A–D). Transition of the frequency of surface reconstruction stripe pitch is also superimposed on panel (a). The colour scale represents frequency increasing from blue to red.

Figure 6(c) shows HSI of $(n \times 3)$ SRTs calculated for each frame of the STMBE images. For each frame of the STMBE sequence, 10 HSI values were calculated for 10 trials of SRT assignments. Since the HSI values depend on SRT assignments, they had variation in one STMBE image. The lower limits of the computed HSI values were over 0.2 whereas the theoretical limit is ~0.14, as stated above. This gap corresponds to the difference between point patterns (a) and (b) in Fig. 1. Interestingly, Fig. 6(c) also shows that the variation of the HSI plots by trials of SRTs assignments become small from ~0.6 ML to ~0.9 ML where the areal density of $(n \times 3)$ SRTs reaches maximum. The distribution of SRTs should, in principle, become more regular with the increasing areal density since SRTs are assigned so that they cannot overlap by more than $1 - P_{OL}$. For example, as seen in Fig. 3(right side column), SRTs were assigned contiguously when the areal density was maximum ($\theta = 0.5$–1.0). It

is notable, however, that the distribution remained definitely non-random when the SRTs decreased in the latter stage of the growth.

C. Growth stages of WL and time evolution of SRTs

The growth of WL can be divided into four stages.

1. Stage A: 0.1–0.2 ML

$(n \times 3)$ regions are beginning to form but are still isolated as ultra-small entities and cannot form SRTs of several nm extent. Figure 6(b) clearly shows that the SRT density is considerably smaller than that expected from the raw spatial occupancy of $(n \times 3)$ regions. The HSI of SRTs and $F(d)$ cannot be reliably calculated at this stage because the number of SRTs is too small. The $F(d)$ was calculated at 0.2 ML InAs coverage. As Fig. 5 shows, this trace indicates that SRTs scatter randomly at this early stage.

2. Stage B: 0.2–0.6 ML

The transition from $c(4 \times 4)$ to $(n \times 3)$ reconstruction on WL surface proceeds quickly ($\sim$10%/0.1 ML) by rapid exchange of substrate Ga atoms and WL In atoms.[28] Figures 6(a) and 6(b) shows that both spatial occupancy and areal density of $(n \times 3)$ are increasing at this stage. This means that $(n \times 3)$ islands grow and join each other to form more SRTs. The trace of $F(d)$ shifts to the left side (Fig. 5), which implies the SRT distribution is becoming regular. Accordingly, the upper limit of the HSI decreased from 0.5 towards 0.3 (Fig. 6(c)). This change corresponds to the regularisation from pattern (e) to pattern (c) in Fig. 1. The regularity is possibly due to physically repulsive forces among SRTs. For example, the $(n \times 3)$ regions have more In atoms intermixed which may induce outward stress fields to surrounding $c(4 \times 4)$ regions.

3. Stage C: 0.6–1.0 ML

Figures 6(a) and 6(b) show that both of the spatial occupancy and the SRT density saturate because almost all of the surface are covered with $(n \times 3)$ surface reconstruction as reported by Prohl *et al.*[30] This is also accounted from the atomic model and the coverage at this stage. SRTs are inevitably assigned contiguous to each other. In this situation, the assignment of SRTs are strongly affected by the restriction that SRTs are not allowed to overlap each other exceeding the limit of $1 - P_{\mathrm{OL}}$. The restriction corresponds to strong "virtual" repulsive forces among SRTs, which considerably contribute to the regular distribution of SRTs. The regularity is indicated by the $F(d)$ trace shifted to the regular side (Fig. 5) and most of the HSI values are below 0.4 throughout this stage (Fig. 6(c)).

4. Stage D: 1.0 ML to QD nucleation

Continuous supply of In atoms gives rise to formation of $(n \times 4)$ regions on the $(n \times 3)$-reconstructed surface. However, the transition from $(n \times 3)$ to $(n \times 4)$ proceeds more slowly (~ -1%/0.1 ML), as seen in Fig. 6(a), since supplied In atoms are not immediately included in the lattice of WL but accumulated on the surface as moving adatoms. This is also known from the fact that step flow growth almost stops at this stage.[16] In spite of the slow transition, the $(n \times 3)$ SRTs density decreases rapidly (Fig. 6(b)), which implies that a small fraction of $(n \times 4)$ perturbs the assignment of $(n \times 3)$ SRTs. Moreover, the variation of the HSI spreads towards the Poisson side (Fig. 6(c)) from 1.0 to 1.1 ML with some plots exceed 0.4. After 1.1 ML the HSI fluctuates and that of QD nucleation sites finally ranges from 0.25 to 0.47. The upper limit is worse and the variation is wider than those of the HSI values (0.28–0.36) at 0.6 ML. This indicates the regularity of $(n \times 3)$ SRTs are perturbed by newly appearing $(n \times 4)$ surface reconstruction.

D. From WL behaviour to QD nucleation

The SRT represents an $(n \times 3)$ region which is the smallest needed for nucleation of a QD, based on the ansatz that QDs preferentially nucleate on $(n \times 3)$. We suppose that the spatial distribution of SRTs accounts for that of QDs. Here, SRTs are assigned on $(n \times 3)$ by a simple MC simulation under restriction of overlapping within $1 - P_{\mathrm{OL}}$. In contrast, the capture zone (CZ) approach[6,31,32] postulates that island nucleation occurs by agglomeration of adatoms followed by growth based on the capture of further adatoms in the Voronoi cell around the island. This suppresses subsequent island nucleation close to an existing island due to the reduced availability of adatoms in the CZ. In fact, the restriction of overlaps discussed above does correspond to the situation that the vicinity of a QD is short of In adatoms so that new QD nucleation is suppressed. The restriction influences the high regularity of SRTs in stage C and is known to affect spatial ordering in the CZ approach.[31,32] The regularity in stage B resembles that of stage C, but as discussed above, the types of originating repulsive interaction is completely different. A CZ-type model could also be used to understand formation of $(n \times 3)$ SRTs. Progress on these ideas would require more data to consider various types of potential forms (both repulsive and attractive, real and virtual) caused by CZ effects, strains,[30,33,34] temperature gradients or Ehrlich-Schwoebel barriers.

The distribution of QDs resembles the regular distribution of SRTs in stage D, which leads to the question of how the spatial distribution of SRTs develops during the growth of WL. The regularity is influenced by the contiguous nature of $(n \times 3)$ SRTs. If the transition from $(n \times 3)$ to $(n \times 4)$ occurred quickly, $(n \times 3)$ regions would be isolated in irregular islands and consequently result in irregular distribution of QDs. In other words, the regularity of SRTs in stage C is *preserved* in stage D and finally results in the regularity of QDs. Because the regularity of $(n \times 3)$ SRTs is more or less perturbed by newly generated $(n \times 4)$, QDs may be nucleated more regularly by more uniform formation of the $(n \times 4)$ regions. This strongly suggests the possibility of regular QD nucleation with the HSI comparable to that of $(n \times 3)$ SRTs at 0.6 ML, depending on WL engineering in stage D.

V. CONCLUSIONS

We have performed HSI analysis on the spatial regularity of surface reconstruction on an $In_xGa_{1-x}As$ WL during epitaxial growth in order to reveal the origin of the regularity on InAs QD formation on GaAs(001). In the correlation between surface reconstruction and consequent QD nucleation sites, we have introduced an idea of SRT, a minimum extent of a surface reconstruction region needed for one QD to nucleate. For each frame of *in situ* STMBE images, $(n \times 3)$ SRTs have been successfully assigned by MC simulation technique. The regularity of SRT distribution and consequent QD distribution is characterised and correlated quantitatively by computing their HSI values. We demonstrate that the HSI sensitively reflects the spatial regularity of SRTs and QD nucleation and that the regularity in QD spatial distribution is traced back to that of $(n \times 3)$ SRTs at the stage as early as 0.6 ML InAs coverage. However, the regularity of $(n \times 3)$ SRTs at 0.6 ML is slightly disturbed by later appearing $(n \times 4)$ surface reconstruction. The HSI can straightforwardly be applied to any experimental or simulation data to evaluate spatial regularity. The derivative of the $F(d)$ cumulative probability function allows more efficient calculation to accurate HSI values and $F(d)$ itself can be computed from the Voronoi tessellation. We have hence shown the usefulness of the HSI to discuss the regularity of the WL surface structure during its growth. If we monitor the HSI *in situ* during WL growth, it may feed back to the growth condition, especially in stage D, to maintain the regularity of stage C which will be succeeded by that of high-density QD nucleation. This control is impossible by using conventional RHEED monitoring which provides types of surface reconstructions and their areal density but not their regularity. As far as we know, this is the first demonstration that a dynamic substrate influences nm-scale nucleation by using the HSI and has broad significance for nucleation and self-assembly. It is also of strong interest to MBE growers and surface scientists seeking to optimise bottom-up semiconductor nanostructure fabrication for high-performance devices.

ACKNOWLEDGMENTS

We are grateful to G. Taylor for assistance in developing the data processing algorithms. G.R.B. is grateful to the Centre for Complexity Science and Centre for Scientific Computing, University of Warwick, for support.

[1]B. Hopkins and J. G. Skellam, Ann. Botany **18**, 213 (1954).
[2]M. Okabe and M. Tanemura, J. Jpn. Stat. Soc. **36**, 121 (2006).
[3]T. Numahara, M. Tanemura, K. Numahara, J. Moriue, Y. Shirahige, I. Yokoi, and Y. Kubota, Forma **24**, 49 (2009).
[4]D. Zahradník, S. Vacek, L. Bílek, I. Nosková, and Z. Vacek, J. For. Sci. **56**, 531 (2010).
[5]M. Einax, W. Dieterich, and P. Maass, Rev. Mod. Phys. **85**, 921 (2013).
[6]G. R. Bell, P. M. Dawson, P. A. Pandey, N. R. Wilson, and P. A. Mulheran, APL Mater. **2**, 012109 (2014).
[7]N. R. Wilson, A. J. Marsden, M. Saghir, C. J. Bromley, R. Schaub, G. Costantini, T. W. White, C. Partridge, A. Barinov, P. Dudin, A. M. Sanchez, J. J. Mudd, M. Walker, and G. R. Bell, Nano Res. **6**, 99 (2013).
[8]Y. Zhang, L. Zhang, and C. Zhou, Acc. Chem. Res. **46**, 2329 (2013).
[9]Y. Arakawa and H. Sakaki, Appl. Phys. Lett. **40**, 939 (1982).
[10]A. Luque and A. Martí, Phys. Rev. Lett. **78**, 5014 (1997).
[11]Y. Okada, R. Oshima, and A. Takata, J. Appl. Phys. **106**, 024306 (2009).
[12]H. Sakaki, Surf. Sci. **267**, 623 (1992).
[13]A. Greilich, S. G. Carter, D. Kim, A. S. Bracker, and D. Gammon, Nat. Photonics **5**, 702 (2011).
[14]T. J. Krzyzewski, P. B. Joyce, G. R. Bell, and T. S. Jones, Surf. Sci. **482–485**, 891 (2001).
[15]S. Tsukamoto and N. Koguchi, J. Cryst. Growth **201–202**, 118 (1999).
[16]S. Tsukamoto, T. Honma, G. R. Bell, A. Ishii, and Y. Arakawa, Small **2**, 386 (2006).
[17]T. Konishi and S. Tsukamoto, Surf. Sci. **605**, L1 (2011).
[18]K. Fujiwara, A. Ishii, and T. Aisaka, Thin Solid Films **464–465**, 35 (2004).
[19]E. Penev, S. Stojkovic, P. Kratzer, and M. Scheffler, Phys. Rev. B **69**, 115335 (2004).
[20]M. Rosini, M. Righi, P. Kratzer, and R. Magri, Phys. Rev. B **79**, 075302 (2009).
[21]H. Eisele, B. Höpfner, C. Prohl, J. Grabowski, and M. Dähne, Surf. Sci. **604**, 283 (2010).
[22]T. Kita, O. Wada, T. Nakayama, and M. Murayama, Phys. Rev. B **66**, 195312 (2002).
[23]J. Grabowski, C. Prohl, B. Höpfner, M. Dähne, and H. Eisele, Appl. Phys. Lett. **95**, 233118 (2009).
[24]K. Yamaguchi, K. Yujobo, and T. Kaizu, Jpn. J. Appl. Phys., Part 2 **39**, L1245 (2000).
[25]J. G. Belk, C. F. McConville, J. L. Sudijono, T. S. Jones, and B. A. Joyce, Surf. Sci. **387**, 213 (1997).
[26]P. A. Bone, J. M. Ripalda, G. R. Bell, and T. S. Jones, Surf. Sci. **600**, 973 (2006).
[27]D. W. Pashley, J. H. Neave, and B. A. Joyce, Surf. Sci. **603**, L1 (2009).
[28]A. Ishii, K. Fujiwara, and T. Aisaka, Appl. Surf. Sci. **216**, 478 (2003).
[29]M. Sauvage-Simkin, Y. Garreau, R. Pinchaux, M. Véron, J. Landesman, and J. Nagle, Phys. Rev. Lett. **75**, 3485 (1995).
[30]C. Prohl, B. Höpfner, J. Grabowski, M. Dähne, and H. Eisele, J. Vac. Sci. Technol. **28**, C5E13 (2010).
[31]P. Mulheran and J. Blackman, Phys. Rev. B **53**, 10261 (1996).
[32]A. Pimpinelli and T. L. Einstein, Phys. Rev. Lett. **99**, 226102 (2007).
[33]T. J. Krzyzewski, P. B. Joyce, G. R. Bell, and T. S. Jones, Surf. Sci. **517**, 8 (2002).
[34]J. Mirecki Millunchick, A. Riposan, B. J. Dall, C. Pearson, and B. G. Orr, Surf. Sci. **550**, 1 (2004).